CrossMark

JM PAPERS

Scale-dependent inclination angle of turbulent structures in stratified atmospheric surface layers

Xuebo Li[1,2], Nicholas Hutchins[2], Xiaojing Zheng[1],†, Ivan Marusic[2] and Woutijn J. Baars[3],†

[1]Center for Particle-Laden Turbulence, Department of Mechanics, Lanzhou University, Lanzhou 730000, PR China

[2]Department of Mechanical Engineering, University of Melbourne, VIC 3010, Australia

[3]Faculty of Aerospace Engineering, Delft University of Technology, 2629 HS, The Netherlands

A large-scale spanwise and wall-normal array of sonic anemometers in the atmospheric surface layer is used to acquire all three components of instantaneous fluctuating velocity as well as temperature in a range of stability conditions. These data permit investigation of the three-dimensional statistical structure of turbulence structures. Based on a similar dataset, Krug *et al.* (*Boundary-Layer Meteorol.*, vol. 172, 2019, pp. 199–214) reported a self-similar range of wall-attached turbulence structures under both unstable and near-neutral stability conditions. They considered only a wall-normal array and thus assessed statistical structure in the wall-normal direction, in relation to the streamwise wavelength. The present work extends the view of a self-similar range of turbulence structures, by including the statistical structure in the spanwise direction. Moreover, by analysing the phase shift between synchronized measurements in the spectral domain, it is inferred how a scale-dependent inclination angle in the streamwise/wall-normal plane varies with stability. Results suggest that the self-similar wall-attached structures have similar aspect ratios between streamwise/wall-normal scales and streamwise/spanwise scales such that $\lambda_x/\Delta z : \lambda_x/\Delta y \approx 1$ for both near-neutral and unstable conditions. Under the most unstable conditions, coherent structures with $\lambda_x/\delta = 1$ are inclined at angles as high as $65°$ relative to the solid boundary, while larger scales $\lambda_x/\delta = 6$ exhibit inclination angles of approximately $35°$. For near-neutral stability conditions, the angle tends towards $12°$ for all scales. It is noted that in the near-neutral condition, the structure inclination angle and the aspect ratio – and thus the statistical modelling of coherent structures in the atmospheric surface layer – are highly sensitive to the value of the stability parameter.

Key words: boundary layer structure, atmospheric flows, stratified turbulence

---

† Email addresses for correspondence: xjzheng@lzu.edu.cn, w.j.baars@tudelft.nl
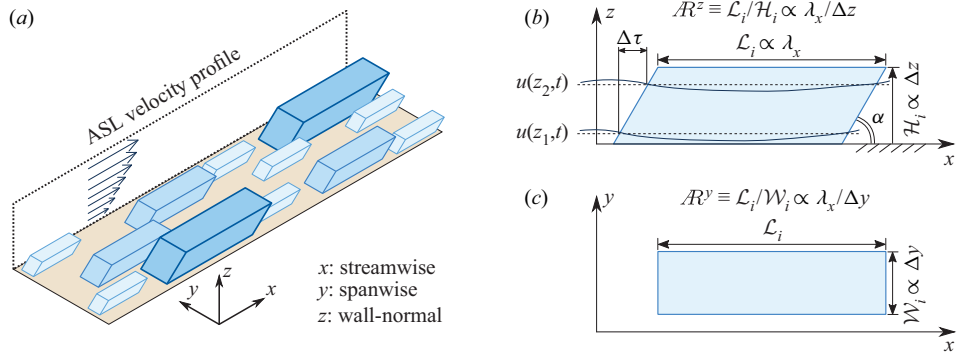
Figure 1. (*a*) Isometric view of three hierarchies of self-similar wall-attached eddies (simplified as slanted cuboids) in the logarithmic region of an ASL. The (*b*) *x*,*z*-plane and (*c*) *x*,*y*-plane of one structure. Here, $\mathcal{L}_i$, $\mathcal{W}_i$ and $\mathcal{H}_i$ denote the streamwise, spanwise and wall-normal extents of the *i*th hierarchy structure.

1. Introduction

Townsend (1976) proposed a conceptual model for wall-bounded turbulence, the attached eddy hypothesis (AEH), which idealizes structures as a collection of inertia-driven self-similar eddies that are distributed randomly in the plane of the wall. Details of key assumptions and limitations associated with the AEH are covered in a recent review by Marusic & Monty (2019). Based on the AEH, Perry & Chong (1982) proposed that coherent wall-attached eddies scale with the distance from the wall z, and their heights comprise a geometrical progression. Evidence in support of self-similarity and wall-scaling of wall-attached vortices has been reported in recent turbulent boundary layer (TBL) studies (e.g. Jiménez 2012; Hwang 2015; Baars, Hutchins & Marusic 2017). Figure 1 shows an idealization of a self-similar hierarchy of wall-attached structures within the logarithmic region of a TBL (Baidya *et al.* 2019; Deshpande, Monty & Marusic 2019; Marusic & Monty 2019). Here, we consider three hierarchy levels of randomly positioned regions of coherent velocity fluctuations, with each hierarchy shown in a different colour. For simplicity, we consider the volume of influence of eddies, in each level, to be characterized by $\mathcal{L}_i$, $\mathcal{W}_i$ and $\mathcal{H}_i$ in the x, y and z directions, respectively, with $i = 1, 2, 3$ denoting the *i*th hierarchy level. Figures 1(*b*) and 1(*c*) depict the aspect ratios in the streamwise/wall-normal plane $\mathcal{R}^z \equiv \mathcal{L}_i/\mathcal{H}_i \propto \lambda_x/\Delta z$ and in the streamwise/spanwise plane $\mathcal{R}^y \equiv \mathcal{L}_i/\mathcal{W}_i \propto \lambda_x/\Delta y$, respectively. Baars *et al.* (2017) reported that in the neutral laboratory zero-pressure gradient TBL, the self-similarity is described by a streamwise/wall-normal aspect ratio $\lambda_x/\Delta z \approx 14$. A recent study by Baidya *et al.* (2019), in high-Reynolds-number pipe and boundary layer flows, indicated that the self-similar wall-attached structures follow the three-dimensional aspect ratio $14 : 1 : 1$ in the streamwise, spanwise and wall-normal directions, respectively. More recently, Krug *et al.* (2019) explored the coherence for both velocity and temperature signals in the atmospheric surface layer (ASL). They found that the streamwise/wall-normal aspect ratio ($\mathcal{R}^z \equiv \lambda_x/\Delta z$) decays with a logarithmic trend with increasing unstable thermal stratification; spanwise information was not explored in their study. Moreover, they found that in the case of stable thermal stratification, the turbulence structures do not adhere to a self-similar scaling, meaning that an aspect ratio is not defined.

Coherent structures reported in TBLs have been associated with characteristic inclination angles because of the mean shear. In the idealized (statistical) view of

figure 1(*b*), inclination angle α in the x,z-plane reflects a phase shift $\Delta\tau$ in time series of velocity fluctuations at different z. Perry & Chong (1982) used a vortex skeleton approach and the Biot–Savart law to determine the inviscid velocity field of a representative eddy, termed the Λ-vortex. In neutral TBLs, hairpin vortices have been invoked commonly as the representative eddy, and Adrian, Meinhart & Tomkins (2000) suggested that these vortices are arranged together in groups called vortex packets. (For a comprehensive review of hairpin structures and their generating mechanisms, see Adrian 2007.) Christensen & Adrian (2001) found that the sequence of individual vortex heads forms an interface or shear layer that is, statistically, inclined away from the wall at angles between $12°$ and $20°$. Laboratory results indicate the most probable inclination angle to be around $10°$–$15°$ (Adrian *et al.* 2000; Christensen & Adrian 2001; Baars, Hutchins & Marusic 2016). In the neutral surface layer, inclination angles ranging from $10°$ to $20°$ have been reported (Boppe, Neu & Shuai 1999; Carper & Porté-Agel 2004; Chauhan *et al.* 2013; Liu, Bo & Liang 2017). Also, Marusic & Heuer (2007) demonstrated the invariance of the inclination angle in wall-bounded flows with zero buoyancy (neutral conditions) over a wide range of Reynolds numbers through laboratory and field experiments. The discussion above pertains to the near-neutral case. However, in studies of the ASL, it has been observed that the inclination angle changes drastically under different stability conditions. The thermal stability of the ASL is generally characterized by the Monin–Obukhov stability parameter z_s/L (Obukhov 1946; Monin & Obukhov 1954), where $L = -u_\tau^3 \bar{\theta}/(\kappa g \overline{w\theta})$ is the Obukhov length, $\kappa = 0.41$ is the von Kármán constant, g is the gravitational acceleration, and $\overline{w\theta}$ is the surface heat flux, with w and θ the fluctuating wall-normal velocity and temperature components, $\bar{\theta}$ the mean temperature, u_τ the friction velocity, and z_s the reference height for evaluating this parameter. Many studies have observed that the inclination angle of coherent structures becomes steeper with increasing unstable thermal stratification (Chauhan *et al.* 2013; Liu *et al.* 2017; Lotfy & Harun 2018). In addition, Chauhan *et al.* (2013) reported that for the case of stable stratification, the statistical inclination angle reduced below the typical values found for the near-neutral case. Recently, Salesky & Anderson (2020*a*) introduced an additional parameter to account for the loading and unloading of surface layer flux–gradient relations imposed by the passage of large-scale motions (LSMs). Meanwhile, Salesky & Anderson (2020*b*) developed a prognostic model for large-scale structures, where the inclination angle is the sum of the inclination angle observed in a neutrally stratified wall-bounded turbulent flow and the stability-dependent inclination angle of the wedge. Baars *et al.* (2016) indicates that in the neutral case, and for all scales $\lambda_x/\delta > 0.5$, the coherent scales obey a virtually constant inclination angle. In unstable conditions in the atmosphere, positive buoyancy lifts the structure away from the surface, leading to an increase in the statistical inclination angle (as averaged across all scales; see Chauhan *et al.* 2013; Liu *et al.* 2017). Now, in the unstable case, the dominance of buoyancy over shear is a function of wall-normal height, hence one expects the inclination angle to be scale-dependent.

Since the coherent structure in the ASL has a strong relationship with the stability parameter, this paper will address specifically the influence of stability on: (1) the streamwise/wall-normal aspect ratio $\mathcal{AR}^z \equiv \lambda_x/\Delta z$ and the streamwise/spanwise aspect ratio $\mathcal{AR}^y \equiv \lambda_x/\Delta y$ in §3.1, and (2) the scale-dependent angle α in §3.2, particularly under unstable conditions. Statistical relations for the aspect ratio and inclination angle for coherent turbulence fluctuations in the ASL are particularly relevant when analysing wind loading in the field of wind engineering (see Davenport 1961, 2002).
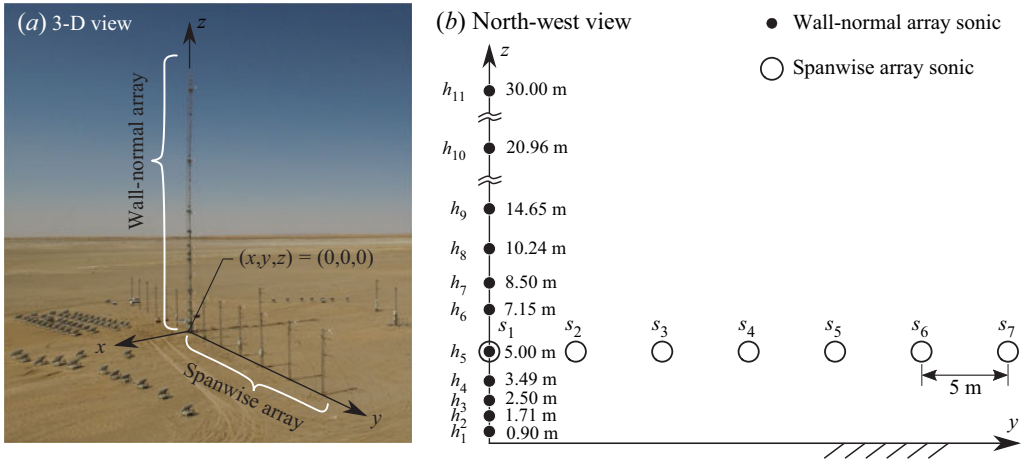
Figure 2. (*a*) Three-dimensional view of the measurement set-up at the QLOA site. (*b*) North-west view of the sonic anemometer array; Campbell CSAT3B and Gill Instruments R3-50 sonics were installed at positions h_1 to h_{11} and s_2 to s_7, respectively.

2. Turbulence dataset of the atmospheric surface layer

2.1. *QLOA facility and available data*

The measurement data used throughout this article were acquired at the QLOA facility in western China, Gansu province, during three-month long measurement campaigns over two years (March to May in 2014 and 2015). The QLOA consists of wall-normal and spanwise arrays of sonic anemometers, performing synchronous measurements of the three-dimensional turbulent flow field. Sonic anemometers (Gill Instruments R3-50 installed from s_2 to s_7, and Campbell CSAT3B installed from h_1 to h_{11}; see figure 2) were employed to acquire time series data of the three components of velocity, as well as the air temperature, at a sampling frequency of 50 Hz. Continuous observations were conducted at the QLOA site for a duration of more than 3000 h, from which 89 h of data were selected to analyse the characteristics of the large-scale coherent structures under different stratification stability conditions. The wall-normal array consists of 11 sonic anemometers that were placed with a logarithmic spacing on a vertical radio-type tower. The spanwise array covered an overall distance of 30 m, with 7 anemometers that were placed at constant height ($z = 5$ m), with an equidistant spanwise spacing of 5 m. The spanwise and wall-normal coordinates for each of the 17 anemometers are provided in figure 2(*b*). It should be noted that the first sonic anemometer in the spanwise array (s_1) also functions as the fifth on the main tower (h_5), which means that we have 7 available anemometers in the spanwise array. The friction velocity u_τ is inferred from $u_\tau = (-\overline{uw})^{1/2}$ at $z = 5$ m (calculated by the mean value from 7 sonic anemometers in the spanwise array). We assume an estimate for the surface layer thickness of $\delta = 60$ m, following Hutchins *et al.* (2012). The 89 h of data remaining after preselection were subdivided into 89 segments of 1 h long time series. This database included 69 h of unstable data ($z_s/L < -0.01$), 10 h of near-neutral data ($-0.01 \leqslant z_s/L < 0.01$), and 10 h of stable data ($z_s/L > 0.01$). Recall that z_s is the reference height used to define the stability parameter z_s/L. For the benefit of comparison with previous works (Chauhan *et al.* 2013; Liu *et al.* 2017; Krug *et al.* 2019), the majority of our work uses $z_s = 2.5$ m, unless otherwise specified. The demarcation of $z_s/L = -0.01$ to distinguish between neutral and unstable thermal stratification is found

commonly in the literature, but for all analysis in this paper, we present results as a function of z_s/L; it will actually be shown later that this demarcation of $z_s/L = -0.01$ is too permissive. The preselection criteria included wind direction (the wind direction had to be aligned with the x axis of the anemometer to within $\pm 30°$) and steadiness (statistically steady conditions based on the high-quality requirement by Foken *et al.* 2005). A de-trending operation is also added (to remove the large-scale synoptic trend). See Hutchins *et al.* (2012) and Wang & Zheng (2016) for full details of the preselection criteria.

2.2. *Processing method*

Two-point correlations can be computed on a per-scale basis in the Fourier domain using the linear coherence spectrum (LCS). For the fluctuating streamwise velocity signals u, the LCS is defined as

$$\gamma_L^2(z, z_{ref}; \lambda_x) \equiv \frac{|\langle \tilde{U}(z; \lambda_x)\, \tilde{U}^*(z_{ref}; \lambda_x)\rangle|^2}{\langle|\tilde{U}(z; \lambda_x)|^2\rangle\langle|\tilde{U}(z_{ref}; \lambda_x)|^2\rangle} = \frac{|\phi'_{uu}(z, z_{ref}; \lambda_x)|^2}{\phi_{uu}(z; \lambda_x)\, \phi_{uu}(z_{ref}; \lambda_x)}. \tag{2.1}$$

Here, $\tilde{U}(z; \lambda_x) = \mathcal{F}[u(z)]$ is the Fourier transform of $u(z)$, in either x or time. The spatio-temporal transformation uses Taylor's hypothesis (Taylor 1938), where the local mean velocity is taken as the convection velocity. The asterisk $*$ indicates the complex conjugate, $\langle\rangle$ denotes ensemble averaging, and $|\ |$ designates the modulus. Scale-dependent phase information is embedded explicitly in the phase of the cross-spectrum ϕ'_{uu}. For (2.1), the LCS is defined based on u at two positions (z_{ref} and z), separated in the wall-normal direction by $\Delta z \equiv z - z_{ref}$. This coherence can also be computed across all other measured signals (v and θ) and also across spanwise separations Δy. The reference signal's height is denoted with the subscript 'ref' and is thus stated as z_{ref}. Since the LCS considers the magnitude of the complex-valued cross-spectrum, only the magnitude of coherence is considered (phase is covered later). Based on assumptions from the AEH (Baars *et al.* 2017; Krug *et al.* 2019), the coherence magnitude within a self-similar region in λ_x, z-space is expected to adhere to

$$\gamma_L^2 = C_1 \ln\left(\frac{\lambda_x}{\Delta z}\right) + C_2, \tag{2.2}$$

from which the statistical aspect ratio (in this case streamwise/wall-normal) then follows:

$$\mathcal{R}^z = \left.\frac{\lambda_x}{\Delta z}\right|_{\gamma_L^2 = 0} = \exp\left(\frac{-C_2}{C_1}\right). \tag{2.3}$$

Here, C_1 and C_2 are fitted parameters. Figure 3 shows an example of data obtained from the ASL to illustrate the process of the coherence spectrum. Figure 3(a) indicates the raw data for the streamwise velocity collected at $h_5 = 5$ m and $h_6 = 7.15$ m, under unstable conditions with $z_s/L = -0.52$. A shorter time history of corresponding filtered signals is shown in figure 3(b), evidencing that signal h_6 leads h_5. Thus a coherent velocity fluctuation is first sensed at the higher wall-normal location as a result of the structure inclination angle. The LCS for h_5 and h_6 is presented in figure 3(c) as a function of temporal frequency, as computed from the 1 h long time series data. Using Taylor's frozen turbulence hypothesis, the frequency axis can be converted to a streamwise wavelength: $\lambda_x \equiv U_c/f$. Here, U_c is a convective speed, taken as the mean velocity at local height z. (The current dataset is fully submerged in the logarithmic region of the ASL.
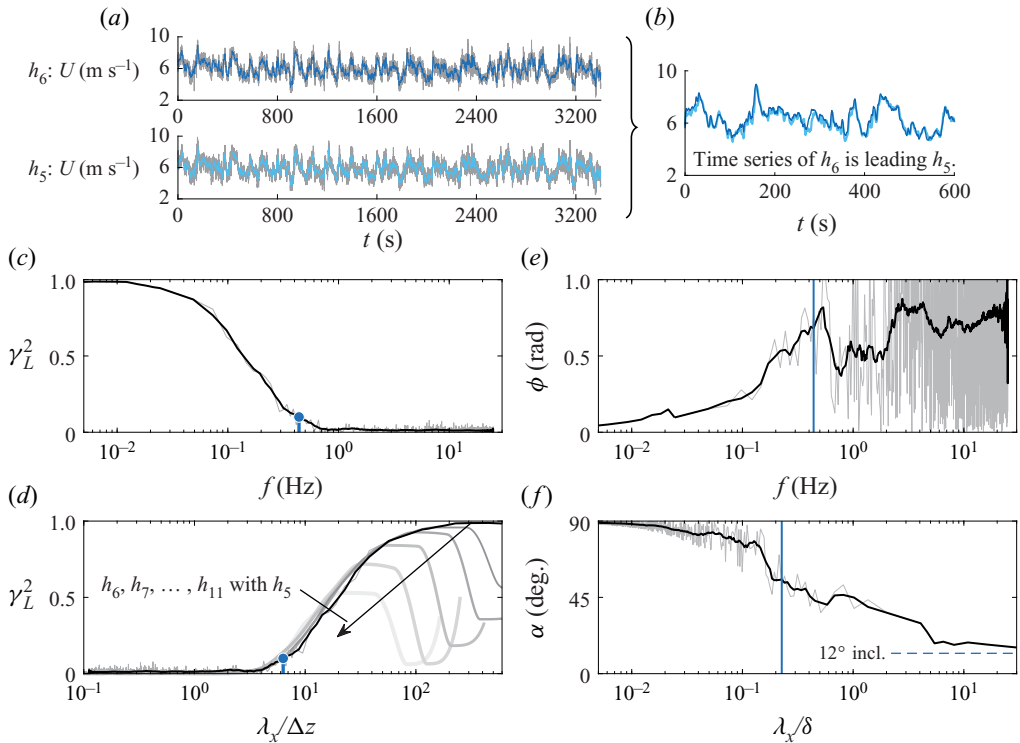
Figure 3. (*a*) An example of time series data for $z_s/L = -0.52$ at heights h_5 and h_6. The blue lines are low-pass filtered at $f = U/\delta$. (*b*) Portion of the filtered signals for inspecting the coherence and time shift. (*c*) Coherence spectrum for height h_6, relative to h_5, as a function of temporal frequency. (*d*) Coherence spectrum for all heights $h_6, \ldots, h_{11}$, again relative to h_5. Here, the abscissa is converted to a spatial wavelength with the mean velocity at height z. (*e*) Scale-dependent phase of the cross-spectrum between h_5 and h_6, which is converted to a physical inclination angle α as a function of a spatial wavelength in (*f*). The blue dots and blue solid lines in (*c*–*f*) indicate the frequency or wavelength corresponding to $\gamma_L^2 = 0.1$. Filtered spectra (black line), overlaid on the grey raw spectra, utilize a bandwidth moving filter of 25 %.

Here, the convective speed of coherent structures agrees well with the mean velocity and is relatively scale-independent (Liu & Gayme 2020). Moreover, Baars *et al.* (2017) showed that when Taylor's hypothesis is used with the local mean velocity $U(z)$, the coherence spectra agree with those computed from spatial DNS data.) The coherence spectrum of figure 3(*c*) can now be presented as a function of the streamwise wavelength, relative to the wall-normal separation distance Δz, as shown in figure 3(*d*). In addition to the coherence spectrum for h_5 and h_6, the coherence spectra for all heights above h_6 (relative to h_5 again) are also shown to illustrate the wall-similarity that is to be investigated. Krug *et al.* (2019) noticed that only data at neutral and unstable thermal stratification conditions complied with (2.2), thus an aspect ratio was found only for those conditions. (A similar conclusion was reached for our QLOA site data, therefore we do not consider stable stratification with $z_s/L > 0$.) In addition, Krug *et al.* (2019) found that the self-similar scaling applies also to fluctuations of the spanwise velocity v and the static temperature θ. Baidya *et al.* (2019) demonstrated that a scaling similar to (2.2) and (2.3) occurs in the spanwise direction, resulting in a streamwise/spanwise aspect ratio $\mathcal{AR}^y$ for the self-similar structure.

942 A38-6

Scale-dependent phase information is embedded explicitly in the phase of the cross-spectrum ϕ'_{uu}, given by

$$\Phi(z, z_{ref}; \lambda_x) = \tan^{-1}\left(\frac{\text{Im}[\phi'_{uu}(z, z_{ref}; \lambda_x)]}{\text{Re}[\phi'_{uu}(z, z_{ref}; \lambda_x)]}\right). \tag{2.4}$$

The phase spectrum aids in assessing the temporal shift between signals. Phase $\Phi(f)$ in (2.4) is shown in figure 3(*e*) and can be used to extract a scale-by-scale inclination angle α (as shown in figure 3*f*). That is, the temporal shift is $\tau = \Phi(f)/(2\pi f)$, where f is the mode frequency, and aids in computing the physical inclination angle through $\alpha = \tan[\Delta z/(\tau U_c)]$. For the spectral analysis, the highest frequency resolved is set by the Nyquist frequency $f_s/2 = 25$ Hz, where $f_s = 50$ Hz is the sampling frequency. The lowest frequency is dictated by the interval length I used in the spectral analysis, and the longest interval used was $I = 2^N$ samples with $N = 15$ (interval length ≈ 650 s). A composite approach with varying interval length ($N = 8, \ldots, 15$) was used to generate the full spectra with as many ensembles as possible for the higher frequency portions of the spectrum (for $N = 8$ a total of around 1000 ensembles were used).

3. Results

3.1. *Stability dependence of aspect ratio*

The linear coherence spectra for u, v and θ as functions of $\lambda_x/\Delta z$ and $\lambda_x/\Delta y$ for the unstable case with $z_s/L = -0.52$ are given in figures 4(*a*) and 4(*c*), respectively. As reported by Krug *et al.* (2019), the LCS collapses on one common curve over a range of $\lambda_x/\Delta z$ and $\lambda_x/\Delta y$. By fitting (2.2) to these regions to obtain C_1 and C_2, the aspect ratio $\mathcal{R}$ can be assessed. For this particular unstable case, we might expect the positive buoyancy to cause the self-similar structures in the hierarchy to lift more aggressively from the wall, extending the wall-normal coherence for a given λ_x scale, hence reducing $\mathcal{R}_u^z$. Indeed, for the unstable case considered in figure 4(*a*), this yields an $\mathcal{R}_u^z$ that is significantly lower ($\mathcal{R}_u^z = 3.6$) than the value $\mathcal{R}_u^z \approx 14$ reported for laboratory neutral conditions (Baars *et al.* 2017) and in close agreement with the aspect ratio reported in Krug *et al.* (2019) for similar values of the stability parameter. The resulting aspect ratios for u, v and θ from all 79 h datasets (covering a range of stabilities from $0.007 \leqslant -z_s/L \leqslant 1.04$) are plotted as functions of the stability parameter in figure 4(*b*) for streamwise/wall-normal aspect ratios $\mathcal{R}^z$, and in figure 4(*d*) for streamwise/spanwise aspect ratios $\mathcal{R}^y$. In all cases, a clear trend emerges between aspect ratio and stability parameter, and a log–linear trend is fitted to the extracted data (black solid curves). These fitted trends are consistent with those of Krug *et al.* (2019) (black dashed curves in figure 4*b*), indicating that the self-similar scaling under near-neutral and unstable conditions is a universal phenomenon. The relatively small differences in the slopes of the solid (current study) and dashed (Krug *et al.* 2019) trend lines, visible in particular for $\mathcal{R}_u^z$ and $\mathcal{R}_\theta^z$, are ascribed to experimental uncertainty in the field measurements: e.g. differences between test sites and the fact that the fitting procedure was performed on a different number of data points, residing at different values of $-z_s/L$. As an extension to the results of Krug *et al.* (2019), the streamwise/spanwise aspect ratios of figure 4(*d*) seem to also exhibit log–linear trends, although in these cases the scatter in results is greater.

Baidya *et al.* (2019) indicates that the aspect ratio is $\mathcal{R}_u^z : \mathcal{R}_u^y = 1 : 1$ in the laboratory neutral condition. The results shown in figures 4(*b,d*) are also supportive of this. For instance, by utilizing the solid trend lines in figures 4(*b,d*), for $\mathcal{R}_u^z$ and $\mathcal{R}_u^y$, respectively,
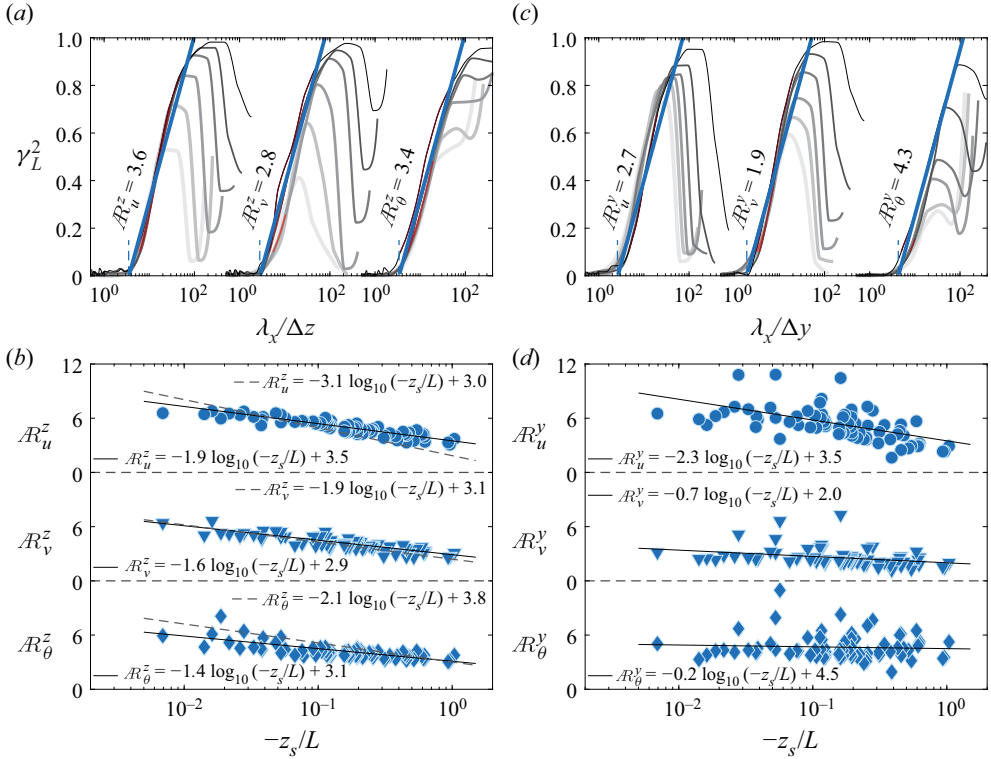
高

Figure 4. Plots of γ_L^2 in the ranges $2.15\,\text{m} \leqslant \Delta z \leqslant 25\,\text{m}$ and $5\,\text{m} \leqslant \Delta y \leqslant 30\,\text{m}$ (with increasing Δz and Δy indicated by lighter shades of grey) for (*a*) the wall-normal coordinate z, and (*c*) the spanwise coordinate y, respectively, for the unstable case with $z_s/L = -0.52$. Here, the ranges are between $\Delta z_{5,6} = h_6 - h_5 = 2.15\,\text{m}$ and $\Delta z_{5,11} = h_{11} - h_5 = 25\,\text{m}$, and between $\Delta y_{1,2} = s_2 - s_1 = 5\,\text{m}$ and $\Delta y_{1,7} = s_7 - s_1 = 30\,\text{m}$. The blue line is a fit to obtain the aspect ratio according to (2.2), with $C_1 = 0.302$ fixed; the fitting region used is bounded by $\gamma_L^2 > 0.1$ and $\lambda_x < 100\,\text{m}$, and is indicated by red lines. Subscript $i = u, v, \theta$ in $\mathcal{R}_i^k$ signifies the aspect ratio for streamwise and spanwise velocity components as well as the temperature component; superscript $k = z, y$ in A_i^k indicates either the streamwise/wall-normal or streamwise/spanwise aspect ratio. (*b,d*) Streamwise/wall-normal and streamwise/spanwise aspect ratios, respectively, as functions of z_s/L. The blue dots are our ASL results, and the black solid lines denote the semi-log fitting. The dashed lines in (*b*) come from Krug *et al.* (2019) with $z_s = 2.14\,\text{m}$ and $z_{ref} = 1.41\,\text{m}$. Note that in this work, $z_{ref} = z_s = 5\,\text{m}$, so the dashed lines of Krug *et al.* (2019) were shifted along the z_s axis to compare the trends at matched $-z_s/L$.

it is found that $\mathcal{R}_u^z : \mathcal{R}_u^y = 0.90 : 1$ for the near-neutral case $z_s/L = -0.01$, and that this ratio changes to $\mathcal{R}_u^z : \mathcal{R}_u^y = 1 : 1$ for a strong unstable stability condition $z_s/L = -1$. By recalling that $\mathcal{R}_u^z \equiv \lambda_x/\Delta z$, the data here indicate that these self-similar eddies for u follow an aspect ratio $\lambda_x : \Delta y : \Delta z \approx 6.4 : 0.90 : 1$ in the near-neutral condition ($z_s/L = -0.01$). It is worth highlighting that again the aspect ratio is sensitive to even very weakly unstable conditions. Therefore, the value for u measured in the ASL is less than the result $\lambda_x/\Delta z = 14$ from Baars *et al.* (2017) and Baidya *et al.* (2019) in neutral laboratory conditions, as was also noticed by Krug *et al.* (2019), whose prediction implies that $\lambda_x/\Delta z = 14$ will be attained only for $|z_s/L| \approx 0.0003$ (but for the current QLOA dataset, we have data only for $|z_s/L| \geqslant 0.007$). Finally, the aspect ratio for u shows that $\lambda_x : \Delta y : \Delta z \approx 4.25 : 1 : 1$ under a more unstable condition ($z_s/L = -1$), demonstrating that positive buoyancy has a lifting effect, increasing the size of coherent structures in the wall-normal and spanwise directions relative to its streamwise extent.

942 A38-8
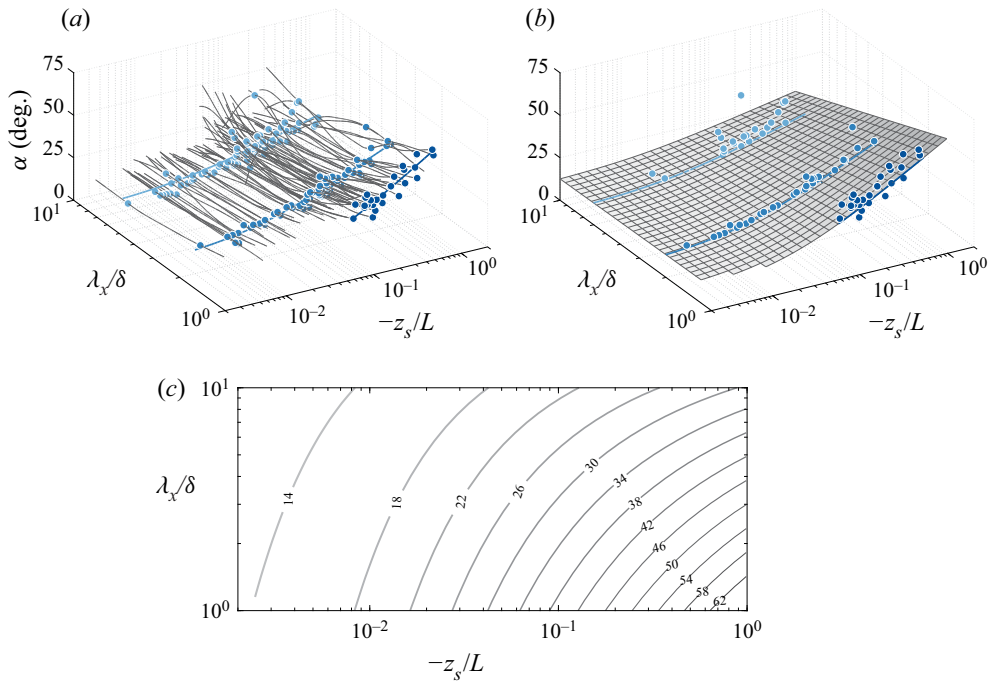
Figure 5. (*a*) The phase expressed as a physical inclination angle α as a function of wavelength λ_x/δ and stability parameter $-z_s/L$. The LCS reference height, $z_{ref} = 0.90$ m, and inclination angles are presented for distances $\Delta z = h_5 - h_1 = 4.1$ m. The solid increasing shades of blue dots indicate the scales at $\lambda_x/\delta = 1$, $\lambda_x/\delta = 2$ and $\lambda_x/\delta = 6$, addressed in detail in figure 6. The solid blue lines show the trend fitted to these data given by (*b*) the surface fit to the data of the form (3.1). (*c*) Similar to (*b*), but now as two-dimensional iso-contours of α as a function of λ_x/δ and $-z_s/L$.

3.2. *Stability dependence of structure inclination angle*

Per the phase spectrum in figure 3(*f*), the scale-dependent phase is now analysed for scales within the range $1 < \lambda_x/\delta < 10$ and for a similar Δz as before, $\Delta z = h_5 - h_1 = 4.1$ m. Larger wavelength information in the phase spectra is prone to noise issues due to the limited ensembles available for constructing the spectra, while smaller wavelengths generally have a lower coherence. Figure 5(*a*) indicates the phase spectra in terms of inclination angle as functions of wavelength λ_x/δ, for all different stability parameters $-z_s/L$. Note that all measured angles in figure 5(*a*) are positive, corresponding to forward-leaning structures. Though there are some clear outliers in these plots, certain trends are visible, as evidenced by the coloured symbols that visualize data at constant scales $\lambda_x/\delta = 1$, 2 and 6. Clearly, these different wavelengths exhibit different dependencies of α with the stability parameter, with $\lambda_x/\delta = 1$ exhibiting much steeper angles α in the most unstable cases, and markedly shallower angles as near-neutrality is approached. In general, it is also noted that longer structures (larger wavelength) will exhibit smaller inclination angles, especially noticeable at stronger convective conditions.

To quantify the trends in the data, a functional form is adopted from Chauhan *et al.* (2013), who used a log–linear trend of convective data in a boundary layer to model the variation of α with stability z_s/L. Note that their angle was inferred from two-point cross-correlation maps and hence is scale-invariant. As such, the only difference is the introduction of a scale-dependent coefficient, here denoted as $C_0 = C_0(\lambda_x/\delta)$ in (3.1).

This function will be illustrated later, but can capture the faster increase of α with increasing $-z_s/L$, for smaller scales. (In the work of Chauhan *et al.* (2013) this coefficient was constant and equaled $C_0 = 7.3$.) So we have

$$\alpha\left(\frac{z_s}{L}, \frac{\lambda_x}{\delta}\right) = \alpha_0 + C_0 \ln\left(1 + 70\left|\frac{z_s}{L}\right|\right). \tag{3.1}$$

The form of (3.1) guarantees that α approaches the invariant value of α_0 when $-z_s/L \to 0$ (here, α_0 is taken as $12°$, and recall that $z_s = 2.5$ m). A curve-fitted plane to those spectra is shown in figure 5(*b*), in which this fit has the form in (3.1); iso-contours of α are depicted in figure 5(*c*), and show that under the most unstable conditions, coherent structures of $\lambda_x/\delta = 1$ are inclined at angles as high as $65°$. It should be noted from figure 5(*a*) that for small near-neutral values of the stability parameter, it is not always possible to compute an inclination angle α for the smaller wavelength ($\lambda_x/\delta = 1$) from the phase spectra since the coherence across Δz drops below $\gamma_L^2 = 0.1$.

Figure 6 shows the variation of α as a function of the stability parameter $-z_s/L$ for three different length scales, $\lambda_x/\delta = 1, 2, 6$. Inclination angles computed from the phase spectra are shown by the coloured circles, and the blue lines show the surface fit to the data given by (3.1). In addition, the black open circles in figure 6, which show the inclination computed from the two-point correlations for all 11 measurement heights, indicate that the current data are consistent with the similarly computed results from Chauhan *et al.* (2013), shown by the black open squares. The black solid line in figure 6 shows the fit proposed by Chauhan *et al.* (2013) based on the two-point correlation contours. As such, this original fit includes all scales, and is skewed disproportionately towards larger-scale features at higher z. It is clear from figure 6 that the increasing buoyancy lifts all scales to larger inclination angles, although the smaller-scale structures considered ($\lambda_x/\delta = 1$) exhibit steeper angles at all values of the stability parameter as compared to the larger features ($\lambda_x/\delta = 6$). This means that the scale-dependent coefficient $C_0 = C_0(\lambda_x/\delta)$ in (3.1) increases systematically as we focus on smaller scales. The coloured curves in figure 6 show the curve fits to the data based on the fit proposed in (3.1), with the constant α_0 and value of the scale-dependent coefficient C_0 given in the figure legend. It should be noted here that for the limited scale range discussed here, $1 < \lambda_x/\delta < 10$, all of these scales are large and associated with the upper end of attached motions and superstructures (Hutchins & Marusic 2007). Although with increasing stability all scales are lifted compared with the neutral condition, the low end of this range ($\lambda_x/\delta = 1$) exhibits the steepest angles, reaching $\alpha \approx 70°$ at $z_s/L = -1.0$. Baars *et al.* (2016) indicated that the inclination angle of the large-scale structures in the neutral laboratory boundary layer is scale-independent with value $\alpha = 14.7°$. Though the data in figure 6 do suggest that α becomes scale-independent in the limit of small $|z_s/L|$, the angle seems to be closer to $\alpha \approx 12°$ for the current data.

The results summarized in figure 6 are computed for a linear coherence spectrum between the reference location $z_{ref} = 0.9$ m and the location $z = 5$ m ($\Delta z = 4.1$ m). In addition, the stability parameter presented on the abscissa of figure 6 is computed based on conditions at $z_s = 2.5$ m. Before considering further the form of the fit described by (3.1), we must consider the sensitivity to z_s, and Δz. Generally, the stability parameter z_s/L depends linearly on height, which would suggest that the scale-dependent structure inclination angles α will also increase with wall-normal height z (since as we move away from the wall, buoyancy effects will increase in dominance relative to shear). To account for this, and to form a stability parameter that better reflects the altitude at which the phase spectrum is evaluated, we propose a fractional stability parameter, dubbed z_F/L, where
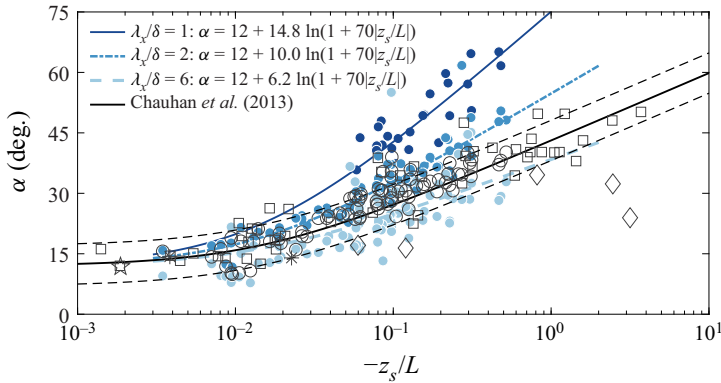
Figure 6. Variation of α with the stability parameter z_s/L ($z_s = 2.5$ m, $z_{ref} = 0.90$ m and $z = 5$ m, so that $\Delta z = 4.1$ m). The solid coloured lines are the fitting lines based on (3.1) for the corresponding scales $\lambda_x/\delta = 1$, 2 and 6. Current data are shown by black circles (based on a two-point correlation, including all scales). The open black squares correspond to near-neutral and unstable ASL data of Chauhan *et al.* (2013); asterisks from $R_{u_\tau u}$ of Marusic & Heuer (2007); diamonds of Carper & Porté-Agel (2004); open pentagram from R_{uu} of Marusic & Heuer (2007).
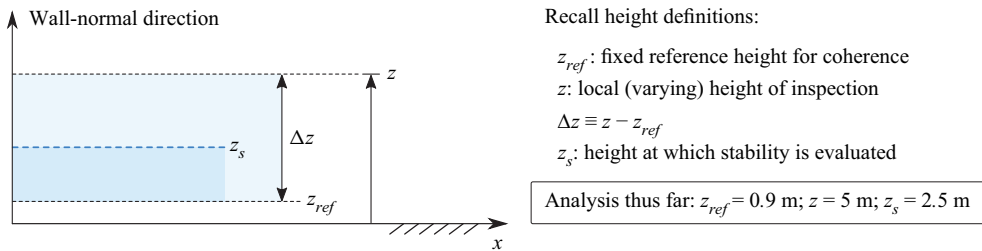

Figure 7. Summary of the different heights involved in the analysis. Heights for which the analyses were performed up to this point are listed in the box.

z_F is fixed at a constant fraction of the wall-normal offset Δz. Hence stability is always assessed at a fixed fractional height between the lower and upper probes used to compute the linear coherence spectrum. This should minimize the sensitivity of the inclination angle–stability parameter relationship to changes in Δz. Since the data in figure 6 are given based on $z_{ref} = 0.90$ m, $z = 5$ m and $z_s = 2.5$ m (figure 7), the fractional stability parameter z_F can be assessed as

$$z_F = \overbrace{\left(\frac{z_s - z_{ref}}{z - z_{ref}} \right)}^{\text{values figure 7}} \Delta z + z_{ref} = 0.39\,\Delta z + z_{ref}. \tag{3.2}$$

Maintaining z_F at the value given by (3.2), when changing Δz or z_{ref}, ensures that we assess stability at the same fractional location $0.39\,\Delta z$ when varying the height of inspection z. We can now substitute z_F for z_s in (3.1):

$$\alpha\left(\frac{z_F}{L}, \frac{\lambda_x}{\delta} \right) = \alpha_0 + C_0 \ln\left(1 + 70 \left| \frac{z_F}{L} \right| \right). \tag{3.3}$$

The grey curves in figure 8(a) show coefficient $C_0 = C_0(\lambda_x/\delta)$ from (3.3), extracted from fits to the data with various Δz. Here, z_{ref} remains fixed at 0.90 m, and z covers
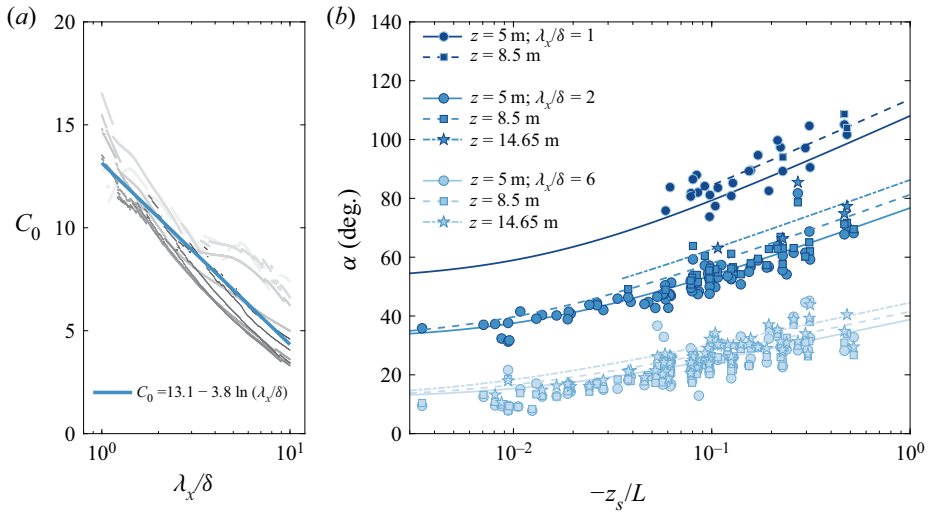
Figure 8. (*a*) Parameter C_0 as a function of wavelength λ_x with increasing Δz indicated by thinner lines and darker shades of grey. Here, z_{ref} remains fixed at $h_1 = 0.91$ m, and z increases from 1.71 m to 30 m (h_2 to h_{11}); the blue solid line indicates a log–linear fit to all grey curves. (*b*) The scale-dependent α for u as a function of stability parameter, for $\lambda_x/\delta = 1, 2, 6$ at h_5, h_7 and h_9 ($z_s = 2.5$ m and $z_{ref} = 0.90$ m); lines come from (3.5), and each set of profiles is offset by $15°$.

all heights above, ranging from 1.71 m to 30 m, with thinner grey lines indicating lower values of z. We can extract α from the phase spectra only in situations where the coherence γ_L^2 is greater than 0.1; this condition gives rise to the sharp drops/rises in figure 8(*a*) as at different λ_x/δ, varying subsets of data are available for the calculation of α. In general, it is noted that the fractional location for the stability height described above does a reasonable job of collapsing the C_0 curves for all Δz; C_0 decreases with λ_x/δ, indicating that the smaller-scale structures tend to have larger inclination angles in the convective conditions. Based on the approximate collapse observed in figure 8(*a*), we can approximate crudely the λ_x/δ dependence of C_0 with

$$C_0 = 13.1 - 3.8 \ln\left(\frac{\lambda_x}{\delta}\right), \tag{3.4}$$

which is shown by the blue solid line in figure 8(*a*). Finally, by combining (3.4) with (3.3), we obtain the scale-dependent structural inclination angle as

$$\alpha\left(\frac{z_F}{L}, \frac{\lambda_x}{\delta}\right) = \alpha_0 + \left(13.1 - 3.8 \ln\left(\frac{\lambda_x}{\delta}\right)\right) \ln\left(1 + 70\left|\frac{z_F}{L}\right|\right). \tag{3.5}$$

Figure 8(*b*) shows the influence of wall-normal offset Δz (with z_{ref} fixed at 0.90 m) on the computed inclination angle α as a function of stability for the wavelengths $\lambda_x/\delta = 1, 2, 6$ for u. A larger Δz leads to higher α, but this can be accounted for by considering the fractional stability parameter. The curves, showing (3.5), describe the variation of α with z_s/L, λ_x/δ and Δz reasonably well.

By way of a summary, figure 9 shows an illustration of the scale-dependent structure inclination angle and aspect ratio for both neutral (subscript *n*) and unstable (subscript *u*) thermal stratification conditions. The illustrations show the streamwise extent of the
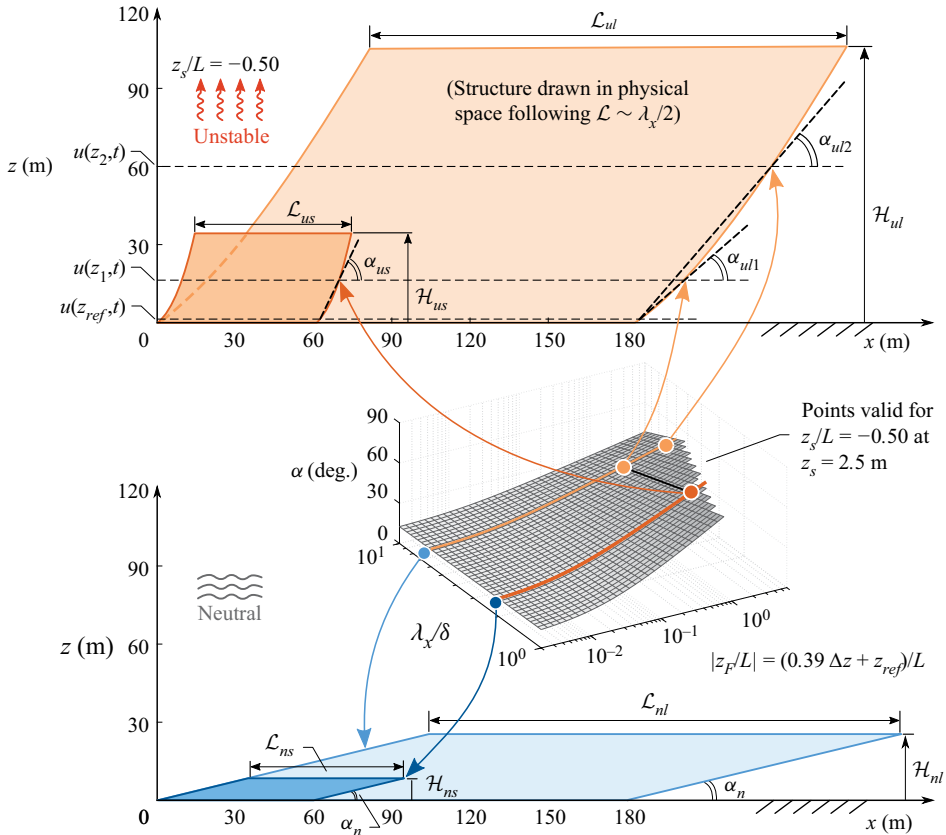
942 A38-12

Figure 9. Summary of aspect ratio $\mathcal{AR}^z$ and scale-dependent angle α in a neutral and unstable stratified ASL. Two hierarchy levels are considered, each of a different scale: $\mathcal{L}$ and $\mathcal{H}$ show the structure's streamwise length and wall-normal height. The subscripts' first letter, n or u, signifies a 'neutral' or 'unstable' condition, and the second designation, s or l, denotes 'small-scale' ($\lambda_x/\delta = 2$) or 'large-scale' ($\lambda_x/\delta = 6$). The dashed lines in the top part indicate a reference location $z_{ref} = 0.90$ m and heights $z_1 = z_{ref} + \Delta z = 15$ m and $z_2 = z_{ref} + \Delta z = 60$ m, for which the corresponding α values are indicated.

structure (in physical space following the simplification that its length $\mathcal{L}$ scales with half the wavelength, thus $\mathcal{L} \sim \lambda_x/2$) and its wall-normal extent with height $\mathcal{H}$; the streamwise/wall-normal aspect ratio of the structure in the x,z-plane adheres to $\mathcal{AR}_u^z$ of figure 4(*b*). When concentrating on the neutral stability condition first (bottom part of figure 9), both scales drawn exhibit the same inclination angle α_n. That is, the statistical inclination angles of large and small scale comprise the same forward leaning behaviour.

When considering unstable thermal stratification – in figure 9, just one value of $z_s/L = -0.50$ is considered, evaluated at $z_s = 2.5$ m – the inclination angle is scale-dependent and also varies with z (the procedure for plotting this structure is summarized in the Appendix). First, note that the coherent wall-attached structures are still self-similar per the definition used in this paper, based on the structure's streamwise wavelength relative to its wall-normal extent. But the aspect ratio reduces compared to the neutral case, and this depends on the degree of thermal stratification per the relations shown in figure 4(*b*), thus $(\mathcal{L}_{ns}/\mathcal{H}_{ns} = \mathcal{L}_{nl}/\mathcal{H}_{nl}) > (\mathcal{L}_{us}/\mathcal{H}_{us} = \mathcal{L}_{ul}/\mathcal{H}_{ul})$. Here, subscripts s and l refer to the small- and large-scale structures visualized, respectively. Concentrating on the inclination

angle (e.g. the phase shift between a reference height z_{ref} and a height of inspection z), it was found that for unstable stratification, it increases with increasing z. Hence $\alpha_{ul2} > \alpha_{ul1}$, and the coherent shape of the structure is characterized by a leading/trailing edge front that is curved and becomes steeper with height. Moreover, smaller-scale structures exhibit steeper angles for the case of equal Δz (e.g. $\alpha_{us} > \alpha_{ul1}$). The trends for this one stability condition are visualized with the 'α-surface' in the centre of figure 9. There, the fractional stability z_F is a surrogate for the Δz trend.

4. Conclusion

Wall-normal and spanwise arrays of sonic anemometers deployed in the atmospheric surface layer enable examination of the linear coherence spectrum, γ_L^2, as a function of the streamwise wavelength (λ_x), spanwise offset (Δy) and wall-normal offset (Δz). This in turn offers the opportunity to explore the three-dimensional form of the wall-attached self-similar structure for the streamwise velocity u, which illustrates that the self-similar wall-attached structures follow an aspect ratio $\lambda_x/\Delta z : \lambda_x/\Delta y \approx 1$ under near-neutral and unstable conditions. It is found that the aspect ratio $\lambda_x/\Delta z$ is greater for the near-neutral case, and becomes progressively smaller as instability increases. Hence similar length (λ_x) structures in unstable conditions will be taller and wider than their near-neutral counterparts. The phase of the cross-spectrum provides a scale-by-scale structure inclination angle. We find that this inclination angle is invariant with scale for the near-neutral case, but with increasing positive buoyancy becomes increasingly scale-dependent. For unstable conditions (e.g. $z_s/L = -0.5$), all scales are inclined at steeper angles compared to the near-neutral case, with the smaller scales with $\lambda_x/\delta = 1$ exhibiting inclination angles that are approximately twice those of larger scales, $\lambda_x/\delta = 6$.

Declaration of interests. The authors report no conflict of interest.

Author ORCIDs.
- Xuebo Li https://orcid.org/0000-0001-7139-8923;
- Nicholas Hutchins https://orcid.org/0000-0003-1599-002X;
- Xiaojing Zheng https://orcid.org/0000-0002-6845-2949;
- Ivan Marusic https://orcid.org/0000-0003-2700-8435;
- Woutijn J. Baars https://orcid.org/0000-0003-1526-3084.

Appendix. Outline of a coherent structure

Visualizing the outline of a coherent statistical structure of a streamwise velocity fluctuation in the streamwise/wall-normal plane relies on a simple model based on (3.5) and (3.2). The procedure for plotting a structure such as the example one in figure 10 involves the following steps.

  (i) A wavelength of the structure should be chosen, i.e. $\lambda_x = 2\delta$. Note that the structure is visualized in physical space, through the assumption that its streamwise extent equals half the wavelength, $\mathcal{L} \sim \lambda_x/2$.
 (ii) A degree of unstable stratification should be chosen, i.e. $z_s/L = -0.40$ (here $z_s = 2.5$ m).
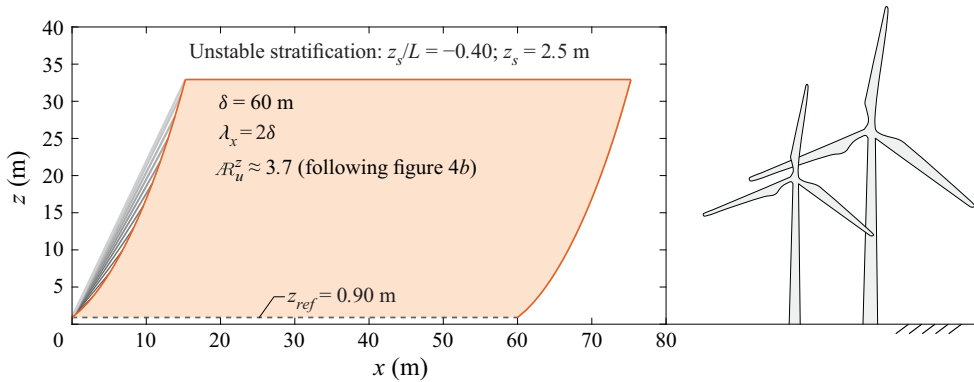(iii) A reference height, above which the structure is visualized, should be chosen.

Figure 10. Example of an outline of a coherent streamwise/wall-normal structure of a particular scale and set of ASL parameters (as indicated in the figure).

A structure outline is then generated through considering a sequence of local heights z. For every height, the angle relative to the fixed reference height is determined from (3.5) and (3.2); this is illustrated by the series of ten grey lines at the left edge of the structure in figure 10. Note that the structure is defined only up to a height that is dictated by the aspect ratio condition, following the trend line in figure 4(*b*). Thus the wall-normal extent up to which the coherent structure reaches is found by computing Δz from $\mathcal{AR}_u^z \equiv \lambda_x / \Delta z = -1.9 \log_{10}(-z_s/L) + 3.5$.

REFERENCES

ADRIAN, R.J. 2007 Hairpin vortex organization in wall turbulence. *Phys. Fluids* **19** (4), 041301.

ADRIAN, R.J., MEINHART, C.D. & TOMKINS, C.D. 2000 Vortex organization in the outer region of the turbulent boundary layer. *J. Fluid Mech.* **422**, 1–54.

BAARS, W.J., HUTCHINS, N. & MARUSIC, I. 2017 Self-similarity of wall-attached turbulence in boundary layers. *J. Fluid Mech.* **823**, R2.

BAARS, W.J., HUTCHINS, N. & MARUSIC, I. 2016 Spectral stochastic estimation of high-Reynolds-number wall-bounded turbulence for a refined inner–outer interaction model. *Phys. Rev. Fluids* **1** (5), 054406.

BAIDYA, R., *et al.* 2019 Simultaneous skin friction and velocity measurements in high Reynolds number pipe and boundary layer flows. *J. Fluid Mech.* **871**, 377–400.

BOPPE, R.S., NEU, W.L. & SHUAI, H. 1999 Large-scale motions in the marine atmospheric surface layer. *Boundary-Layer Meteorol.* **92** (2), 165–183.

CARPER, M.A. & PORTÉ-AGEL, F. 2004 The role of coherent structures in subfilter-scale dissipation of turbulence measured in the atmospheric surface layer. *J. Turbul.* **5**, N40.

CHAUHAN, K., HUTCHINS, N., MONTY, J. & MARUSIC, I. 2013 Structure inclination angles in the convective atmospheric surface layer. *Boundary-Layer Meteorol.* **147** (1), 41–50.

CHRISTENSEN, K.T. & ADRIAN, R.J. 2001 Statistical evidence of hairpin vortex packets in wall turbulence. *J. Fluid Mech.* **431**, 433–443.

DAVENPORT, A.G. 1961 A statistical approach to the treatment of wind loading on tall masts and suspension bridges. PhD thesis, Department of Civil Engineering, University of Bristol, UK.

DAVENPORT, A.G. 2002 Past, present and future of wind engineering. *J. Wind Engng Ind. Aerodyn.* **90** (12), 1371–1380.

DESHPANDE, R., MONTY, J. & MARUSIC, I. 2019 Streamwise inclination angle of large wall-attached structures in turbulent boundary layers. *J. Fluid Mech.* **877**, R4.

FOKEN, T., GÖOCKEDE, M., MAUDER, M., MAHRT, L., AMIRO, B. & MUNGER, W. 2005 *Post-Field Data Quality Control*, pp. 181–208. Springer.

HUTCHINS, N., CHAUHAN, K., MARUSIC, I., MONTY, J. & KLEWICKI, J. 2012 Towards reconciling the large-scale structure of turbulent boundary layers in the atmosphere and laboratory. *Boundary-Layer Meteorol.* **145** (2), 273–306.

HUTCHINS, N. & MARUSIC, I. 2007 Evidence of very long meandering features in the logarithmic region of turbulent boundary layers. *J. Fluid Mech.* **579**, 1–28.

HWANG, Y. 2015 Statistical structure of self-sustaining attached eddies in turbulent channel flow. *J. Fluid Mech.* **767**, 254–289.

JIMÉNEZ, J. 2012 Cascades in wall-bounded turbulence. *Annu. Rev. Fluid Mech.* **44**, 27–45.

KRUG, D., BAARS, W.J., HUTCHINS, N. & MARUSIC, I. 2019 Vertical coherence of turbulence in the atmospheric surface layer: connecting the hypotheses of Townsend and Davenport. *Boundary-Layer Meteorol.* **172**, 199–214.

LIU, C. & GAYME, D.F. 2020 An input–output based analysis of convective velocity in turbulent channels. *J. Fluid Mech.* **888**, A32.

LIU, H., BO, T. & LIANG, Y. 2017 The variation of large-scale structure inclination angles in high Reynolds number atmospheric surface layers. *Phys. Fluids* **29** (3), 035104.

LOTFY, E.R. & HARUN, Z. 2018 Effect of atmospheric boundary layer stability on the inclination angle of turbulence coherent structures. *Environ. Fluid Mech.* **18** (3), 637–659.

MARUSIC, I. & HEUER, W.D. 2007 Reynolds number invariance of the structure inclination angle in wall turbulence. *Phys. Rev. Lett.* **99** (11), 114504.

MARUSIC, I. & MONTY, J. 2019 Attached eddy model of wall turbulence. *Annu. Rev. Fluid Mech.* **51**, 49–74.

MONIN, A.S. & OBUKHOV, A.M. 1954 Basic laws of turbulent mixing in the surface layer of the atmosphere. *Contrib. Geophys. Inst. Acad. Sci. USSR* **151** (163), e187.

OBUKHOV, A.M. 1946 Turbulence in an atmosphere with inhomogeneous temperature. *Inst. Teor. Geofis. Akad. Nauk SSSR* **1**, 95–115.

PERRY, A.E. & CHONG, M.S. 1982 On the mechanism of wall turbulence. *J. Fluid Mech.* **119**, 173–217.

SALESKY, S.T. & ANDERSON, W. 2020*a* Coherent structures modulate atmospheric surface layer flux–gradient relationships. *Phys. Rev. Lett.* **125**, 124501.

SALESKY, S.T. & ANDERSON, W. 2020*b* Revisiting inclination of large-scale motions in unstably stratified channel flow. *J. Fluid Mech.* **884**, R5.

TAYLOR, G.I. 1938 The spectrum of turbulence. *Proc. R. Soc. Lond.* A **164** (919), 476–490.

TOWNSEND, A.A. 1976 *The Structure of Turbulent Shear Flow*. Cambridge University Press.

WANG, G. & ZHENG, X. 2016 Very large scale motions in the atmospheric surface layer: a field investigation. *J. Fluid Mech.* **802**, 464–489.